

Article

LCNS Positioning of a Lunar Surface Rover Using a DEM Based Altitude Constraint

Floor Thomas Melman ^{1,†} , Paolo Zoccarato ¹, Csilla Orgel ¹, Richard Swinden ¹, Pietro Giordano ¹ and Javier Ventura-Traveset ²

¹ European Space Research and Technology Centre (ESTEC), European Space Agency

² Centre Spacial de Toulouse, European Space Agency

* Correspondence: Floor.Melman@esa.int; Tel.: +31-7156-53522

† Current address: European Space Research and Technology Centre (ESTEC), European Space Agency, Noordwijk, Netherlands

Abstract: With the renewed interest for lunar surface exploration, the European Space Agency envisions to stimulate the creation of lunar communications and navigation services (LCNS) to enable, among others, autonomous navigation capabilities for lunar rovers. As the number of satellites foreseen in such a service is much smaller compared to Earth based global navigation satellite systems (GNSS), different complementary technologies are pursued to improve the attainable navigation accuracy for lunar rovers. One way to improve the position accuracy provided by the LCNS satellites is to constrain the vertical position using a high resolution digital elevation model (DEM). This article presents the results of a variance covariance analysis of an extended Kalman filter (EKF) implementation in which the LCNS ranging measurements are used together with DEM from the LRO LOLA instrument. Assuming a realistic orbit determination and time synchronization (ODTS) accuracy of the LCNS satellites, the usage of a navigation grade IMU and an oven controlled crystal oscillator (OCXO), a 3-sigma position accuracy of less than 10 meters can be obtained. Furthermore, the availability is substantially improved as the DEM aided solution enables a position solution in case of only 3 visible satellites.

Keywords: DEM; LCNS; Moonlight; Traverse; Navigation



Citation: Melman, F.T.; Zoccarato, P.; Orgel, C.; Swinden, R.D.; Giordano, P.; Ventura-Traveset, J. LCNS Positioning of a Lunar Surface Rover Using a DEM Based Altitude Constraint. *Preprints* **2022**, *1*, 0. <https://doi.org/>

Publisher's Note: MDPI stays neutral with regard to jurisdictional claims in published maps and institutional affiliations.



Copyright: © 2022 by the authors. Licensee MDPI, Basel, Switzerland. This article is an open access article distributed under the terms and conditions of the Creative Commons Attribution (CC BY) license (<https://creativecommons.org/licenses/by/4.0/>).

1. Introduction

The interest for lunar exploration has grown significantly in the past years, both at institutional and commercial level [1]. The Earth based techniques currently adopted for communication and navigation with satellites in cislunar space are not able to cover all the needs for future exploration, both in terms of service accessibility (South Pole and far side are not always accessible by Earth based ground stations) and service performances (i.e. need to land within 100 meters of a predetermined location on the lunar surface [2]). The European Space Agency's vision, represented in the Moonlight initiative [3], is to stimulate the creation and development of lunar communications and navigation services (LCNS), to be delivered by private partners, that will support the next generation of institutional and private Lunar Exploration Missions, including the enhancement of the performance for those missions currently under definition.

Several other space agencies and commercial entities have proposed dedicated systems to offer communication and navigation services within the (cis)lunar service volume. In US, Lockheed Martin has proposed Parsec [4]. JAXA (Japan Aerospace Exploration Agency) has recently launched a study which will consider possible lunar positioning satellite systems [5]. Roscosmos has announced a concept that envisions the deployment of a lunar satellite navigation system between 2036 and 2040 [6]. Finally, China recently announced that its space agency (CNSA) is planning to set up a satellite constellation around the Moon to provide communication and navigation services [7]. On top of these initiatives, NASA has proposed the LunaNet framework to enable interoperability among different lunar communication and navigation service providers [8].

The challenge of accurate navigation for lunar surface users (i.e. rovers) has been of interest since the early robotic explorations of the Moon [9] and typically relies on technologies such dead-reckoning where inertial navigation sensors (INS) [10], wheel odometry and visual odometry (VO) [11–13] are used for terrain relative localization. The advantage of visual navigation is its passive nature [14] (as it uses visual light) and that the imagery can be used for hazard avoidance and traverse planning [15]. Dead-reckoning technologies, however, are not suitable for long traverses as the error grows without bounds [16]. For absolute positioning, planetary rovers relied "ground-in-the-loop" (GITL) processing of down-link images in which on-board images were interactively registered (i.e. mapping between local and global maps) to orbital imagery [17]. Such an approach, however, is impractical for autonomously operated vehicles. Furthermore, the attainable absolute accuracy is determined by the resolution of the global (orbital) maps [18]. Nevertheless, recent developments may allow autonomous processing and registering of global and local imagery or 3D point clouds [15].

Rover images can also be used to derive local digital elevation models (DEM). When the global DEMs are available on-board the rover, they can be correlated against local DEMs to provide a global position [19]. However, variation in the solar illumination angle may lead to a change in the terrain appearance which complicates the image registration [17]. LIDAR (light detection and ranging) can be used to remove the dependency on surface illumination conditions [16]. Tests on Earth in a Mars-Moon analogue environment when using 3D LIDAR scans for matching against a 3D orbital map for global navigation (complemented by visual odometry and an inclinometer/sun-sensor) resulted in position errors smaller than 100 meter [16]. Finally, craters can be used as landmarks to yield a global navigation solution [17] obtaining high positioning accuracies (5 to 10 meter). Nevertheless, the position accuracy is determined by, among others, the size of the crater and illumination conditions.

Alternatively, rovers can use radio frequency (RF) tracking techniques [20]. Current radiometric tracking of surface users relies mostly on direct to Earth link that has some intrinsic limitations. First of all the impossibility to serve far side missions. In addition, serving one user at a time substantially limits the autonomy of assets on the lunar surface. To overcome this issue, several studies have been considering dedicated lunar navigation systems [18,20,21] consisting of 1 or 2 satellites (potentially complemented by a pseudolite or reference station on the lunar surface) to augment the previously (e.g. visual odometry) mentioned technologies. As demonstrated in [18], using a joint Doppler and ranging approach (JDR), a relative (with respect to a reference station) positioning accuracy of 10-15 meters can be obtained using 2 satellites and a surface beacon. An absolute accuracy of 100 meters can be obtained globally after processing 2 hours of observations. The LiASON (Linked Autonomous Interplanetary Satellite Orbit Navigation) concept exploits inter-satellite link range and range-rate data to compute relative and inertial absolute positioning obtaining a navigation accuracy of 150 meters (1-sigma) using the inter-satellite links alone. While adding 4 hours of daily DSN (deep space network) observations positioning a navigation accuracy on the order of 10 meter can be achieved [21].

A dedicated Lunar Communication and Navigation Service (LCNS), such as the one proposed within the ESA Moonlight initiative, would provide several advantages over the previously mentioned technologies. First of all, its performance is not dependent on illumination conditions. This is important as rovers may need to traverse permanently shadowed regions on the lunar South Pole [22] as these may contain water ice [23]. Secondly, it would improve the autonomy of the rover as it passively uses the LCNS signals in one-way ranging mode (i.e. it will not actively use resources of the LCNS satellites for navigation purposes). Thirdly, the navigation accuracy is not governed by size and shape of features that are used to register local and global maps. Finally, the positioning accuracy is only marginally impacted by the accuracy of available maps (e.g. DEM's and feature maps).

This paper presents the results of a covariance analysis covering the navigation performances achievable by a lunar rover using the Moonlight navigation service as received

by a Moonlight user together with inertial measurement units (IMU) and digital elevation models (DEM) information. This contribution considers a lunar traverse covering the South Pole. The considered algorithm is based on an Extended Kalman Filter (EKF) in which the altitude is constrained (with respect to the lunar ellipsoid) by the DEM available on-board the rover, allowing for complete autonomy from ground operations. The uncertainty of the DEM is monitored considering the uncertainty of the DEM (due to interpolation and orbital errors) and the uncertainty of the rover position (which can result in a large altitude uncertainty near the edge of a crater). Thanks to detailed maps generated by the measurements performed by the LOLA (Lunar Orbiter Laser Altimeter) instrument [24] flying in the Lunar Reconnaissance Orbiter (LRO) [25], DEM's (digital elevation models) are available covering the South Pole at a resolution of 5 meters per pixel and a geolocation uncertainty of 10 – 20 cm horizontally and 2 -4 cm vertically [26].

This paper is structured as follows. Section 2 provides an overview of the lunar rover traverse used and its characteristics. Section 3 describes the LCNS constellation considered in this publication as well as the characteristics of the rover, including the satellite orbits, payload characteristics and rover receiver. Section 4 addresses the mathematical formulation of the covariance analysis. Section 5 reports the results of the simulations and Section 6 provides the conclusive remarks.

2. Lunar Surface Rover Mission Profile

The rover traverse selected for this paper is based on literature [22] and circumnavigates the de Gerlache crater in an anti-clockwise direction (see Figure 1). With a total length of 320 km, expected to be covered in about 11 days by a pressurized rover with an average speed of 5 km/h (operated by humans) [22], this traverse has been chosen to cover areas of scientific interest and present two major technical advantages: first the slopes encountered in the traverse are manageable by the actual rovers (i.e. lower than 25 degrees) and second the traverse is covered by high resolution DEMs. This paper only considers a small portion of this traverse, which coincides with one of the high resolution lunar DEMs [26]. The portion of the traverse considered in this publication is highlighted in Figure 1 with a black square. From this point forward the term "traverse" is used to refer to this small portion of the overall traverse proposed in [22]

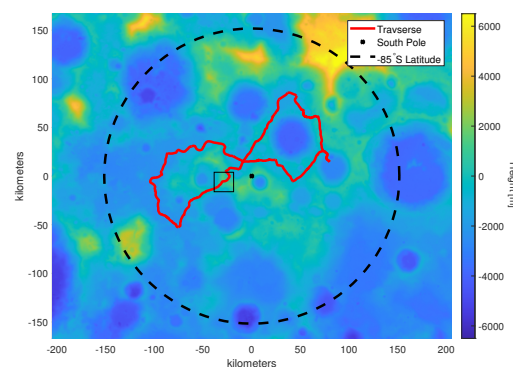


Figure 1. Lunar South Pole traverse. The full DEM is provided at a resolution of 100 meter/pixel [27], while the small square indicates the region for which a high resolution DEM at 5 meter/pixel is available. Projection is polar stereographic where (0,0) denotes the South Pole.

A remotely operated rover was chosen for this study, with a maximum speed of 0.36 km/h [22] (which is representative of tele-robotic operation), contrary to the 5 km/h which was considered by [22] for a small pressurized rover (SPR), leading to a completion of the traverse portion (as bounded by the black square in Figure 1) in about 3 days. The two-dimensional traverse was converted to a three-dimensional traverse sampled at a rate of 1 Hz by considering a maximum horizontal velocity of 0.36 km/h using the following steps:

1. Loading the 2D traverse [22] provided in a geographic information system (GIS) shapefile.
2. Time tag the points along the traverse such that the horizontal velocity equals 0.36 km/h.
3. Interpolating the horizontal traverse at the requested time-step (1 s).
4. Interpolating the DEM to get the rover position in polar stereographic reference frame (including the height). As the velocity is horizontally constrained, the actual velocity in three dimensions will be slightly larger than 0.36 km/h.
5. Converting the polar stereographic coordinates to a selenodetic reference frame.

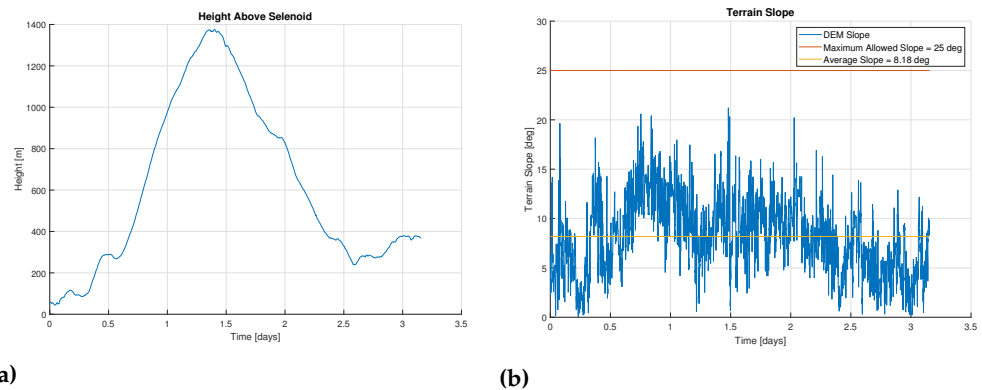


Figure 2. Rover altitude profile within the coverage of the high resolution DEM. (a) shows the rover height above the Selenoid, while (b) shows the slope given by the DEM.

Figure 2 shows the elevation and slope along the traverse with the time in days covering a distance of approximately 27 km and a height ascent of 1300 meters. The maximum slope encountered is 21.2 degrees while the average slope is 8.2 degrees. The traverse was loaded into the ESA Lunar Navigation Simulator [28,29] to acquire the link data with the LCNS satellites. The simulation environment used in the publication considered also the terrain data provided on the NASA planetary data system (PDS) archive and generated by the lunar orbiter laser altimeter (LOLA) [30]. In this way the simulation accounts also for the local topographic and related signal occultations (see Figure 3 (a) for the implementation of the traverse in the simulation environment).

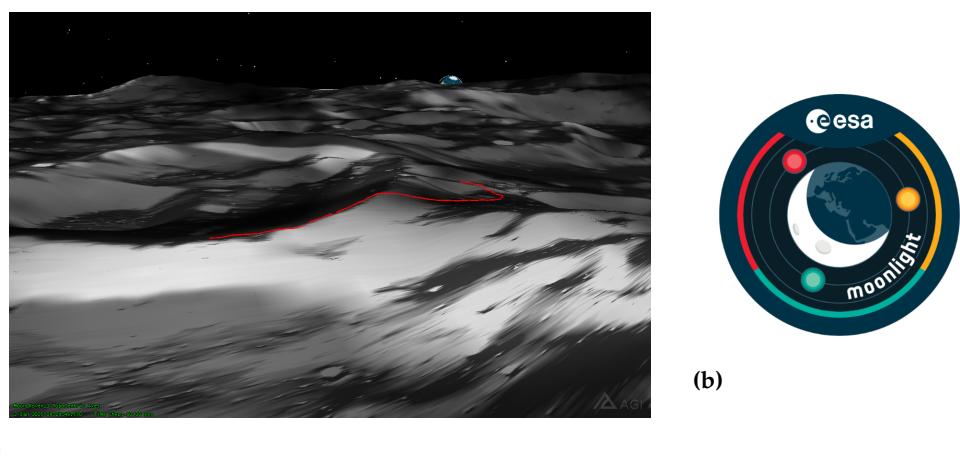


Figure 3. (a) Part of the lunar traverse shown in Figure 1 considered in this paper. The terrain topography shown is based on the high resolution DEM provided (5 meter/pixel) in the LOLA PDS archive [30]. The left part of the traverse follows the southern rim of the de Gerlache crater, while the right part descends into the direction of the Shackleton crater. (b) shows the Moonlight Logo.

3. Moonlight and LCNS

The Moonlight navigation service (see Figure 3 (b) for the mission logo) aims to provide a one-way broadcast radio navigation signal to allow a user to compute its position, velocity and time, similarly as done for GNSS (e.g. the signals broadcasted by the Moonlight satellites will be synchronized among them). This concept has been presented in the past (e.g. [31]), but now Moonlight can take advantage of the significant evolution of GNSS technologies both at satellite/system and user level. In fact, the Moonlight navigation concept aims to extensively and intentionally reuse GNSS technology in order to achieve fast time to market (the current target is to provide the first services in 2027-2028 time frame) and ease the introduction of the concept within future lunar missions by means of reuse of already existing spaceborne GNSS receivers with minimum modifications. This is achieved implementing GNSS modulations, navigation techniques and technologies. This concept has been embraced by the NASA LunaNet framework and called Lunar Augmented Navigation Service (LANS) [8].

ESA defined 3 phases to establish a lunar radio navigation service:

- **Phase 1 - Use of High-sensitivity space Receivers (2022-2025):** Based on the reception of Earth GNSS signals with high-sensitivity receivers, on-board dynamic filters and high-gain antennas. This phase should provide initial services for the Earth-Moon transfers and lunar orbit operations.
- **Phase 2 - Lunar Communication and Navigation Services (LCNS) (2025-2035):** Enhancing the Phase 1 with the transmission of additional ranging signals from both the Moon orbit and surface. This phase should allow a major reduction of the geometric DOP (dilution of precision) and improve the service availability, which, in turn, would translate into enhanced lunar orbit navigation and initial landing/surface PNT (position, navigation and timing) services (e.g. on the Moon South Pole).
- **Phase 3 - Full Lunar PNT system (2035-onwards):** This Phase should provide PNT services on the whole Moon surface and enhance the positioning availability and accuracy on Moon orbit and lunar South Pole. This could be obtained by complementing Phase 2 with additional lunar orbiting satellites and Moon surface beacons. This phase could also allow for the provision of integrity services for safety critical applications, leading to increased autonomy.

This contribution focuses on how Phase 2 (LCNS) could support rover surface operations.

Two parallel Phase A/B1 studies are ongoing at the moment to define the Moonlight system, therefore this contribution does not aim to provide the definitive constellation or characteristics, but rather to provide an example of what can be achieved with such system. The results provided in this contribution are considered representative of the future system, even if the actual constellation might not be identical to the one used here.

As mentioned in previous publications [29,32,33], at least during Phase 2 of the Moonlight navigation roadmap, the navigation service will not be able to serve users in every location all the time. Given the limited number of satellites on the initial LCNS constellation (see Section 3.1), the navigation service will be provided in specific time slots for a specific area of the lunar surface. For this reason, user mission analysts will have to plan the critical operations (e.g. final descent of a lunar lander) based on the predicted availability of the service. This process has been described in details in [29] and [33] and it is used accordingly in this contribution.

3.1. LCNS Constellation

The LCNS constellation considered in this paper is comprised of four satellites in elliptical lunar frozen orbits (ELFOs). These orbits are highly eccentric and have their argument of perilune (i.e. the point at which spacecraft in lunar orbit is closest to the Moon) close to the Moon's North Pole to ensure maximum coverage above the Moon's South Pole. The four satellites are located in two different planes, wherein the satellites in the first

plane are separated by 123.4° and the satellites in the second plane by 180°. The orbital parameters are provided in Table 1.

Table 1. Kepler elements of the LCNS ELFO orbits. Note that the orbits have not been optimised and are therefore not representative of the Moonlight orbits.

Satellite Number	Semi-major axis	Eccentricity	Inclination	Argument of pericenter	RAAN	True Anomaly
1	9,750.73 km	0.6383	54.33°	55.18°	277.53°	123.42°
2	9,750.73 km	0.6383	54.33°	55.18°	277.53°	0°
3	9,750.73 km	0.6383	61.96°	121.7°	59.27°	180°
4	9,750.73 km	0.6383	61.96°	121.7°	59.27°	0°

The constellation parameters in this publication have been derived by ESA based on internal studies, but these may be further optimised. Better performances are indeed expected with the constellation provided in the Phase A/B1 studies currently ongoing.

3.2. LCNS Payload

The navigation payload in the LCNS satellites is responsible for broadcasting the one-way ranging signals to the lunar users. Contrary to the Earth, the Moon does not have a significant atmosphere removing the need for a dual frequency broadcasting. Furthermore, to avoid potential interference with Earth GNSS L-band signals (which may be used up to Lunar altitudes [28]) and in line with SFCG (space frequency coordination group) R32 recommendation [34], the signals are transmitted using the S-band carrier frequency (2491.005 MHz). Finally, to keep the receiver implementation simple (note that lunar users may use both LCNS and Earth GNSS), a simple BPSK(5) (binary phase shift keying) modulation is used (similarly to the Galileo E6BC signal). The signal characteristics are summarized in Table 2.

Table 2. Characteristics of the proposed LCNS signal.

Element	Parameter	Value
Signal Carrier	Carrier Frequency (f_s)	2491.005 MHz
	Carrier Wavelength (λ_s)	12.04 cm
Signal Modulation	Chipping Frequency (f_C)	BPSK(5)
	Chip Length (λ_C)	58.61 m

The LCNS antenna boresight is pointed towards the centre of the Moon (i.e. nadir pointing). As the distance between the surface and the Moon and the LCNS satellites is relatively small (compared to the Earth GNSS case), the EIRP (effective isotropic radiated power) can be kept small and is considered to be 15.02 dBW at boresight. The LCNS transmission antenna pattern is considered symmetric and the off-boresight EIRP is provided in Figure 4. The transmission antenna pattern considered in this publication is based on internal ESA studies and aims to provide an example of a more representative pattern compared to previous publications from the same authors [29,33,35]. It is important to note that the final antenna patterns for LCNS are currently under assessment within the Phase A/B1 studies and are expected to be provide similar (or better) performances.

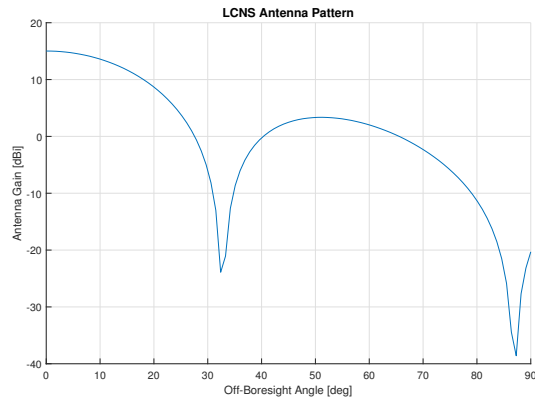


Figure 4. Antenna pattern of the LCNS satellites.

3.3. Rover LCNS Receiver

In line with previous works [29,33], the lunar surface rover will be equipped with a LCNS receiver which can be modelled similarly to a space-borne GNSS receiver. Such a receiver is comprised of a radio frequency front-end (RFFE) and digital parts for signal processing. The main difference with respect to a GNSS receiver will be the change of carrier frequency from L-band to S-band, the rest will be almost identical.

The receiver is expected to rely on state-of-the-art tracking techniques using a DLL (delay locked loop) and PLL (phase locked loop). Within the simulation environment used in this contribution a hard acquisition and a C/N_0 (carrier-to-noise density ratio) tracking threshold at 30 dB-Hz was selected (in line with [29]). Any signal with a C/N_0 below this threshold is considered not acquired nor tracked. This is an arbitrary decision that will be revisited as part of the Phase A/B1 and that drives the overall link budget and payload EIRP. For the scope of this publication the threshold is considered achievable with current state of the art technology at user level. The RFFE noise figure has been set to 1 dB, which should be line with state-of-the-art products for space applications [29]. Finally, the noise temperature is set to 113 K (based on internal ESA assessment, this value will be re-assessed in future publications) and the LNA gain to 30 dB. All receiver parameters are summarized in Table 3.

Table 3. Characteristics of the rover LCNS S-band receiver.

Parameter	Value
RF Front-end Noise Figure	1 dB
Noise Temperature	113 K
LNA Gain	30 dB
C/N_0 cutoff	30 dB-Hz

The antenna of the rover is assumed to be pointing in the zenith direction (i.e. upwards). This assumes an ideal case when the rover moves on a flat surface. In reality the antenna pointing will vary with the slope of the local terrain. The impact of this assumption, however, is considered small (i.e. note a gain variation of 1 dBi in Figure 5 between zenith and an off-boresight angle of 20 degrees). The receiver antenna is assumed to be symmetric in azimuth and the elevation pattern is visualized in Figure 5, which is considered representative of what is currently available on the market for space-borne GNSS antennas. Similar performances are achievable in S-band. No elevation mask is implemented, however lunar terrain in the vicinity of the traverse (refer to Section 2) was considered to evaluate the impact of the local topography on the visibility between the rover and the LCNS satellites.

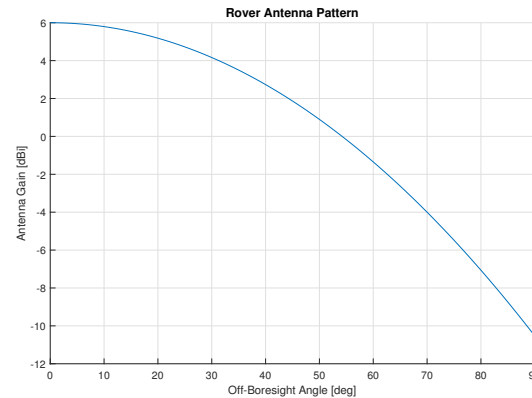


Figure 5. Antenna pattern of the receiver.

The navigation system of the LCNS receiver will be complemented by an inertial measurement unit (IMU). Within this study a tactical grade IMU similar to the LN200S [36] is considered which has been used by the most recent NASA Mars rovers (i.e. Spirit, Opportunity, Curiosity and Perseverance). Within this study the impact of the IMU is not directly modelled, however its contribution is accounted for in the definition of the process noise of the extended Kalman filter (for more details refer to Section 4 or previous publications [29]). Table 4 provides examples of the characteristics of different grades of IMU's. The process noise indicated in Table 4 will be used to define the process noise in the simulation as further detailed in Section 4.4.

Table 4. Examples of different types of space grade IMU's and their characteristics (cost values from [37], other specifications from the respective datasheet). Note that the velocity process noise considers a conservative integration time of 1 second.

	Navigation Grade	Tactical Grade
Cost	>50kEUR	10-20 kEUR
Weight	9.0 kg	748 g
Example	iMAR iNAV-RQH-1001 [38]	Northrop Grumman LN-200S [36]
Velocity Random Walk	$8 \mu\text{g}/\sqrt{\text{Hz}}$	$35 \mu\text{g}/\sqrt{\text{Hz}}$
Velocity Process Noise (σ_v)	$7.8 \cdot 10^{-5} \text{m/s}/\sqrt{\text{s}}$	$3.4 \cdot 10^{-4} \text{m/s}/\sqrt{\text{s}}$

The clock of the navigation receiver is expected to be an oven controlled crystal oscillator (OCXO). The characteristics of such a clock type and it's impact of the process noise can be found in Table 5. The process noise indicated in Table 5 will be used to define the process noise in the simulation as further detailed in Section 4.4.

Table 5. Examples of space grade OCXO clocks.

Product	Microchip OX-249 [39]	AXTAL AXIOM6060 [40]	AXTAL AXIOM70SL [41]
Weight	14 grams	200 grams	20 grams
Reference frequency	n/a	100 MHz	10 MHz
Frequency Stability	100 ppb	50 ppb	10 ppb
Allan Deviation ($\tau = 1 \text{ s}$)	$1 \cdot 10^{-11}$	$1 \cdot 10^{-10}$	$5 \cdot 10^{-12}$
Clock Bias			
Process Noise (σ_{δ_t})	$0.003 \text{ m}/\sqrt{\text{s}}$	$0.030 \text{ m}/\sqrt{\text{s}}$	$0.001 \text{ m}/\sqrt{\text{s}}$
Clock Drift			
Process Noise (σ_{δ_t})	$30 \text{ m/s}/\sqrt{\text{s}}$	$15 \text{ m/s}/\sqrt{\text{s}}$	$3 \text{ m/s}/\sqrt{\text{s}}$

4. Covariance Analysis

4.1. Extended Kalman Filter

The positioning engine in the LCNS receiver will implement an EKF. Similarly as for surface users on Earth, the estimation is kinematic (i.e. the position is propagated only by the velocity). For further details regarding the extended Kalman filter and its derivation, the reader is referred to existing literature [42,43]. In this paper, a variance-covariance analysis is employed, meaning that the states are not actually estimated, but only the effect of the measurement errors and geometry on the EKF solution is assessed. The equations that are used to propagate and predict the covariance of the state vector are given below.

The state vector contains 8 elements and is given in Equation 1. where \mathbf{r} denotes the 3D position vector in a Moon fixed reference frame, $\dot{\mathbf{r}}$ the 3D velocity, dt denotes the receiver clock bias and \dot{dt} the receiver clock drift.

$$\mathbf{x} = \begin{bmatrix} \mathbf{r} \\ \dot{\mathbf{r}} \\ dt \\ \dot{dt} \end{bmatrix} \quad (1)$$

Equation 2 shows how the propagated state covariance matrix $P_{k|k-1}$ is evaluated, where $F_{k-1,k}$ denotes the state transition matrix, Γ the process noise transition matrix and Q_{k-1} the process noise covariance matrix. Note that the first part of the subscript $k|k-1$ refers to the state propagation, while the second part of the subscript refers to the state update using the measurements. Therefore $P_{k|k-1}$ denotes the covariance matrix of the state vector that is propagated in epoch k and updated in epoch $k-1$. Note that in real operations, the initial covariance P_0 will be estimated using the weighted least squares (WLS) algorithm. In this paper, however, we assume a fixed value for P_0 which is further detailed in Section 4.4.

$$P_{k|k-1} = F_{k-1,k} P_{k-1|k-1} F_{k-1,k}^T + \Gamma Q \Gamma^T \quad (2)$$

Equation 3 shows the definition of the Kalman gain matrix. Note that H_k denotes the design (or measurement) matrix (which is defined in Section 4.3) while Σ_k denotes the measurement covariance matrix (which is defined in Section 4.3).

$$K_k = P_{k|k-1} H_k^T (H_k P_{k|k-1} H_k^T + \Sigma_k)^{-1} \quad (3)$$

Equation 4 shows the definition of the state covariance update step using the Bucy-Jopseh formulation (note that I denotes the 8x8 identity matrix). This formulation has been selected as it ensures P_k is symmetric.

$$P_{k|k} = (I - K_k H_k) P_{k|k-1} (I - K_k H_k)^T + K_k \Sigma_k K_k^T \quad (4)$$

4.2. Prediction Model

The prediction model is selected in alignment with previous works [29] and represents the dynamics of the lunar rover. As previously discussed in Section 4.1, a simple kinematic model was selected assuming a uniform motion such that the propagation of the rover position at epoch k is based on the estimation of its velocity at epoch $k-1$. The state transition matrix (or propagation model) is shown in Equation 5.

$$F = \begin{bmatrix} I_{3 \times 3} & I_{3 \times 3} \cdot \Delta T & & \\ & I_{3 \times 3} & & \\ & & 1 & \Delta T \\ & & & 1 \end{bmatrix} \quad (5)$$

Whereas the state transition matrix assumes a linear motion profile, the motion of the rover will be non-uniform. This mismodelling is considered in the propagation step by

adding additional uncertainty by means of the process noise matrix Q which is defined in Equation 6.

$$Q = \begin{bmatrix} I_{3 \times 3} \cdot \sigma_p^2 & & & \\ & I_{3 \times 3} \cdot \sigma_v^2 & & \\ & & \sigma_{\delta t} & \\ & & & \sigma_{\delta t} \end{bmatrix} \quad (6)$$

To account for the length of the propagation time-step (ΔT), the process noise transition matrix Γ (as defined in Equation 7) is used. In this paper, however, the propagation time-step is considered to be 1 second, such that Γ is equal to the identity matrix.

$$\Gamma = \begin{bmatrix} I_{3 \times 3} \cdot \Delta T & & & \\ & I_{3 \times 3} \cdot \Delta T & & \\ & & \Delta T & \\ & & & \Delta T \end{bmatrix} \quad (7)$$

The definition of the process noise (by means of the parameters σ_p , σ_v , $\sigma_{\delta t}$ and $\sigma_{\delta t}$) plays an important role in the final accuracy that can be achieved. Therefore, this paper performs a sensitivity study using different process noise values to assess the impact on the attainable position accuracy.

4.3. Measurement Model Model

The mathematical model for the covariance analysis adapted in this paper is based on previous works [29] (to which the reader is referred for a full derivation). The design matrix H is repeated here and completed with the DEM measurement for completeness in Equation 8.

$$H = \begin{bmatrix} H_p \\ H_{\dot{p}} \\ H_{DEM} \end{bmatrix} = \begin{bmatrix} -\frac{\mathbf{r}_r^{1T}}{\|\mathbf{r}_r^1\|} & \mathbf{0}^T & 1 & 0 \\ \vdots & \vdots & \vdots & \vdots \\ -\frac{\mathbf{r}_r^{mT}}{\|\mathbf{r}_r^m\|} & \mathbf{0}^T & 1 & 0 \\ -\frac{(\mathbf{i}_r^1 - (\mathbf{i}_r^1 \mathbf{u}_r^1) \mathbf{u}_r^1)^T}{\|\mathbf{r}_r^1\|} & -\frac{\mathbf{r}_r^{1T}}{\|\mathbf{r}_r^1\|} & 0 & 1 \\ \vdots & \vdots & \vdots & \vdots \\ -\frac{(\mathbf{i}_r^m - (\mathbf{i}_r^m \mathbf{u}_r^m) \mathbf{u}_r^m)^T}{\|\mathbf{r}_r^m\|} & -\frac{\mathbf{r}_r^{mT}}{\|\mathbf{r}_r^m\|} & 1 & 0 \\ \frac{\mathbf{r}_r^{DEM T}}{\|\mathbf{r}_r^{DEM}\|} & \mathbf{0}^T & 0 & 0 \end{bmatrix} \quad (8)$$

Note that this model represents the case where at least 4 satellites are visible such that the rank of the design matrix H is equal or larger than the number of states. However, in case only 3 satellites are visible and one DEM measurement is available, the rank of the design matrix is 7 while the number of states is equal to 8 (note that a DEM range-rate measurement would not be realistic as the DEM resolution is 5 meter per pixel and the rover moves at a velocity of 0.1 meter per second). Therefore, in the case of 3 available satellites, the LCNS range-rate measurements are disabled meaning $H_{\dot{p}}$ in Equation 8 is removed. In such case, only position is estimated directly, while the velocity of the rover is propagated through the dynamical model.

4.4. Simulation Settings

Table 6 shows the main configuration settings for the covariance analysis grouped in three sets of parameters: LCNS ODTs uncertainty (which drives the SISE - Signal in Space Error), the EKF process noise (which drives the definition of the process noise matrix Q defined in Equation 6) and the initial state covariance of the EKF (which defines P_0).

The ODTS uncertainty is selected to be in line with the parameters provided by previous work [29,33], which are considered achievable at maximum age-of-data (AOD) (AOD is defined in line with the Galileo service definition document (SDD) [44]). This parameter represents the system contribution to the user ranging error (also known as User Equivalent Range Error, UERE). In this study, the ODTS uncertainty is considered to be the same in each direction (i.e. radial, tangential and along-track) and therefore the uncertainties provided in Table 6 are directly mapped to the line-of-sight. This is clearly a simplification that aims to provide an upper bound of the performances. Two parallel studies to gain more insight into the ODTS uncertainty that can be achieved for a lunar navigation system are currently running at ESA. The outcomes of these studies will be taken into account in further studies to allow for a more realistic estimation of the SISE.

Table 6. Configuration settings used for the EKF covariance analysis, all values are 1-sigma.

Parameter	State Vector Element	Value
LCNS ODTS Uncertainty (1-sigma)	Position ($\sigma_{sv,p}$)	15 m
	Velocity ($\sigma_{sv,v}$)	0.15 m/s
	Clock ($\sigma_{sv,\delta t}$)	10 m
	Clock drift ($\sigma_{sv,\dot{\delta t}}$)	0.1 m/s
EKF Process Noise (1-sigma)	Position (σ_p)	$0.01 \text{ m}/\sqrt{s}$
	Velocity (σ_v)	$0.15 \text{ m/s}/\sqrt{s}$
	Clock ($\sigma_{\delta t}$)	$1 \text{ m}/\sqrt{s}$
	Clock drift ($\sigma_{\dot{\delta t}}$)	$10 \text{ m/s}/\sqrt{s}$
Initial EKF Uncertainty (1-sigma)	Position	100 m
	Velocity	10 m/s
	Clock	100 m
	Clock drift	1 m/s

Similarly to the ODTS uncertainty, the EKF process noise is selected being in line with previous works [29,33]. However, the magnitude of the clock process noise is adapted, and a higher process noise is associated to the clock drift (as this parameter drives the propagation of the clock bias). Furthermore, in this publication the process noise related to the clock bias and drift is driven by the Allan deviation and frequency stability respectively assuming an OCXO (details on the Allan deviation and frequency stability of an OCXO are provided in Table 5). The process noise for the clock bias is set to $1 \text{ m}/\sqrt{s}$ which is conservative considering the expected Allan deviation for an OCXO. The process noise for the clock drift is set to $10 \text{ m/s}/\sqrt{s}$ which is within the spectrum of expected frequency stability seen for actual OCXO's (refer to Table 5).

The process noise for the position and velocity is kept in line with previous works [33]. It has been shown that a velocity estimation with an accuracy of better than 1 cm/s is achievable using a tactical grade IMU [45]. Therefore, the process noise provided in Table 6 is considered conservative. The process noise of $0.15 \text{ m/s}/\sqrt{s}$ is in line with a LCNS only solution considering the maximum rover velocity of 0.1 m/s. To understand how the positioning accuracy can be improved while using a tactical or navigation grade IMU, a sensitivity analysis is performed using different process noise values (related to the different IMU types reported in Table 4) for the position and velocity components as further detailed in Section 5.3.

Finally, the initial EKF position uncertainty is set to 100 meters. This value seems realistic considering the work performed in previous publications [29,33,35] that demonstrated that the use of LCNS could lead to landing accuracies well within 100 meters 3-sigma. In addition the rover initial position could be estimated over time using different techniques (LCNS, visual odometry, Earth tracking, etc), allowing to have an initial position uncertainty well within 100m. The velocity initial uncertainty is set to 10 m/s which is considered conservative as the rover will not move faster than 0.1 m/s. The clock bias and drift initial uncertainty are selected in line with previous works [29,33].

4.5. Measurement Covariance Modelling

The measurement covariance matrix Σ_k (used in the evaluation of the Kalman gain matrix as shown in Equation 3) is defined in Equation 9. Note that the size of matrices Σ_{pp} and $\Sigma_{\dot{p}\dot{p}}$ is $m \times m$ where m is the number of visible LCNS satellites. Σ_{pp} and $\Sigma_{\dot{p}\dot{p}}$ are further defined in Section 4.5.1. Furthermore, the definition of σ_{DEM} and n are provided in Section 4.5.2.

$$\Sigma_k = \begin{bmatrix} \Sigma_{pp} & 0 & 0 \\ 0 & \Sigma_{\dot{p}\dot{p}} & 0 \\ 0 & 0 & n\sigma_{DEM} \end{bmatrix} \quad (9)$$

4.5.1. LCNS Covariance Model

The uncertainty of the LCNS measurements due to thermal noise can be modelled using the same methodology as for Earth GNSS assuming the pseudorange noise is determined by the DLL, while the pseudorange-rate measurements are determined by the FLL. The uncertainty can be modelled using Equations 10 and 11 for respectively the pseudorange and pseudorange-rate [46].

$$\sigma_{DLL} = \lambda_C \sqrt{\frac{B_{DLL}d}{2C/N_0} \left(1 + \frac{2}{T_i C/N_0(2-d)}\right)} \quad (10)$$

$$\sigma_{FLL} = \frac{\lambda_S}{2\pi T_i} \sqrt{\frac{4B_{FLL}}{C/N_0} \left(1 + \frac{1}{T_i C/N_0}\right)} \quad (11)$$

The parameters used in those equations (i.e. settings of the DLL and FLL) are provided in Table 7, while the signal characteristics are given in Table 2.

Table 7. Configuration settings used for the EKF covariance analysis.

Parameter	Value
DLL Loop bandwidth (B_{DLL})	0.5 Hz
FLL Loop bandwidth (B_{FLL})	10 Hz
Coherent Integration (T_i)	20 ms
Early-late spacing (d)	1 chip

The C/N_0 (carrier-to-noise density ratio in dB-Hz) is evaluated considering a complete link budget from satellite to receiver including the transmission and reception antenna pattern using the ESA Lunar Navigation simulator used also in previous publications (e.g. [28]).

The definition of Σ_{pp} and $\Sigma_{\dot{p}\dot{p}}$ is given in Equation 12 and 13 respectively considering the uncertainty at tracking level as well as the accuracy of the LCNS ODS (note that $\sigma_{sv,p}$ and $\sigma_{sv,v}$ respectively represent the satellite position and velocity uncertainty while $\sigma_{sv,\delta t}$ and $\sigma_{sv,\delta t}$ respectively present the satellite clock bias and drift).

$$\Sigma_{pp} = \begin{bmatrix} (\sigma_{DLL,1}^2 + \sigma_{sv,p} + \sigma_{sv,\delta t}) & & \\ & \ddots & \\ & & (\sigma_{DLL,m}^2 + \sigma_{sv,p} + \sigma_{sv,\delta t}) \end{bmatrix} \quad (12)$$

$$\Sigma_{\dot{p}\dot{p}} = \begin{bmatrix} (\sigma_{PLL,1}^2 + \sigma_{sv,v} + \sigma_{sv,\delta t}) & & \\ & \ddots & \\ & & (\sigma_{PLL,m}^2 + \sigma_{sv,v} + \sigma_{sv,\delta t}) \end{bmatrix} \quad (13)$$

4.5.2. DEM Covariance Model

The uncertainty of the DEM measurement is governed by three terms:

1. The data component which is related to the orbital errors and interpolation.
2. A geologic component which is related to natural terrain variations (e.g. variation of the terrain within one pixel).
3. A component which is related to horizontal covariance of the receiver of the rover. When the covariance of the rover is larger than 5 meters (i.e. the width of a pixel), the rover can also be located in adjacent pixels which introduces an additional uncertainty component in the height measurement.

The first term (data component) is related to the geolocation uncertainty of the ground track. By iteratively adjusting the LOLA tracks to the LOLA-based DEM in a self consistent fashion [26] the orbital geolocation errors can be reduced by a factor of 10 such that the ground track geolocation accuracy is 10-20 cm horizontally and 2-4 cm vertically. Furthermore, methods are available [26] to estimate the surface height uncertainty in the DEMs, accounting for the reduced orbital errors and interpolation errors by assuming the fractal¹ behaviour of the small-scale topography. This information is available for each DEM pixel.

Figure 8 (a) shows the surface height uncertainty related to the data component (accounting for the reduced orbital errors and interpolation errors). Note that the orbital tracks can be clearly observed as for these pixels the uncertainty is low (i.e. low interpolation error). The bright areas in Figure 8 (a) represent areas for which the interpolation error is large. Figure 8 (b) shows the histogram representing the altitude error due to orbital and interpolation errors. Most of the pixels have an error between 0 and 1 meter.

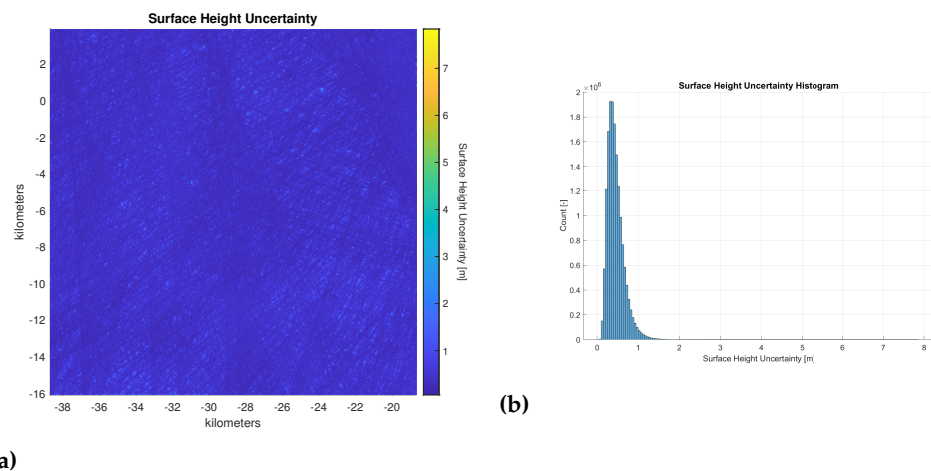


Figure 6. Surface Height Uncertainty (σ_{Data}). **(a)** shows the surface height uncertainty [26] related to the data component for each pixel of the DEM (Projection is polar stereographic where (0,0) denotes the South Pole), while **(b)** shows the histogram for all pixels shown in **(a)**.

The second term (geological component) is related to natural terrain variations and sub-pixel sampling (i.e. variation of the terrain within one pixel that cannot be captured in the DEM). This error is typically larger than the geolocation uncertainty [26]. To capture the magnitude of this error, detailed sub-pixel information is required (i.e. to detect the presence of rocks and boulders). As this information is not available, the 3-sigma covariance is used in the variance covariance analysis for the DEM measurement (note that the 1-sigma is shown in Equation 14), accounting implicitly for this uncertainty.

The third term is related to the uncertainty of the rover. In an ideal scenario the receiver uncertainty would be zero such that the right DEM pixel (and the associated height) could

¹ In the geological context, fractal behaviour means that new details will emerge when a feature is observed more closely

be selected and only data and geological errors remain. However, in a realistic scenario the uncertainty of the receiver is non-zero and as such the selected pixel (based on the current receiver position) may not be correct. Depending on the variation of the terrain and the receiver uncertainty this error may attain significant values (e.g. at the edge of a cliff).

Figure 7 shows conceptually how the uncertainty of the rover is used to evaluate the associated uncertainty in the DEM measurement. It is assumed that the rover location (after the EKF propagation step) is somewhere in the pixel denoted with R_x . However, depending on the receiver horizontal covariance (denoted by σ_{2D}), the receiver may be actually located in another pixel with a different height. For example, assuming a horizontal receiver uncertainty of $\sigma_{2D} = 9$ m and a DEM resolution of 5 meters per pixel, it means that the rover can be in any of the pixels indicated by 1-9. Subsequently, the standard deviation of all these pixels is used to evaluate the rover contribution to the uncertainty of the DEM measurement. Note that only the pixels for which the distance between the center of that pixel and the center of the pixel denoted with R_x is less than σ_{2D} are used to evaluate σ_{rx} . It is assumed that this approach will give a first order estimate on the accuracy of the DEM measurement. A more complicated approach (e.g. considering the position history to select more probable pixels) can be considered for future work. However, in case the rover uncertainty is below 5 meters (equal to the resolution of the DEM), at least the surrounding pixels (see Figure 7, pixels indicated 1-9) are used to compute the standard deviation, as rover may be located in any of these pixels.

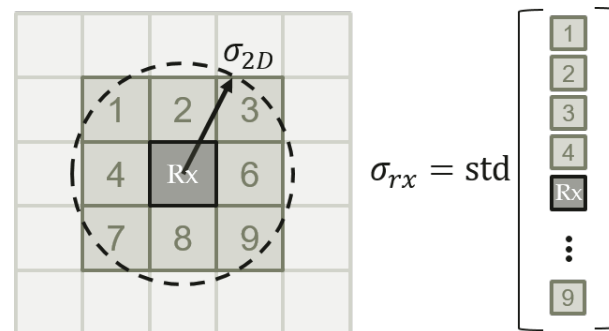


Figure 7. Conceptual drawing showing how the uncertainty related to the DEM measurement is evaluated based on the rover horizontal uncertainty.

Figure 8 (a) and (b) show the standard deviation of the terrain surrounding each pixel considering a rover uncertainty (1σ) of respectively 10 meter and 100 meters. Figure 8 (a) shows that a rover uncertainty of 10 meters leads to a surrounding terrain standard deviation not larger than 8 meters, and actually much lower along the actual traverse. A 100 meter receiver uncertainty leads to a surrounding terrain standard deviation up to 25-30 meters (Figure 8 (b)). The actual traverse shows lower values (below 15 meters), confirming the good selection of the traverse (e.g. far from steep cliffs).

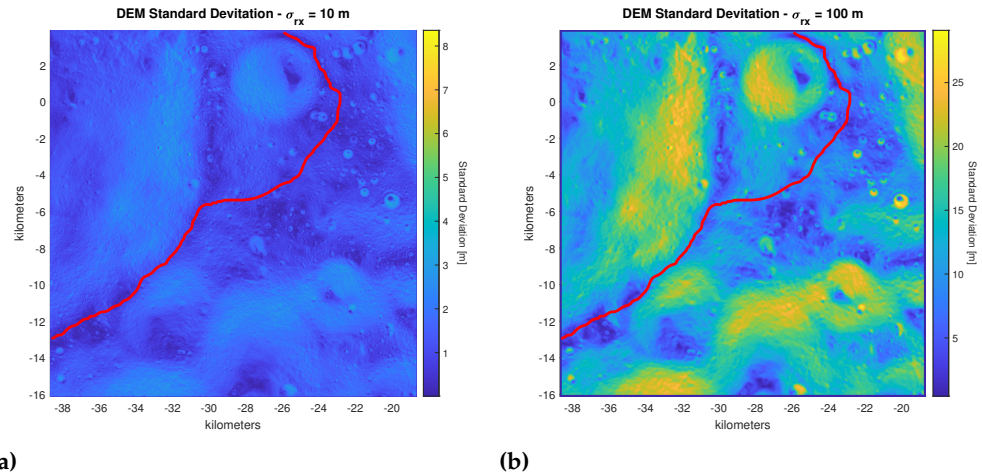


Figure 8. Standard deviation (σ_{rx}) of the lunar terrain surrounding the rover traverse (in red). **(a)** shows the standard deviation of the terrain height considering all pixels which have their centre within 10 meter of the query point, while **(b)** shows the standard deviation for all pixels which have their centre within 100 meter of the query point. Projection is polar stereographic where (0,0) denotes the South Pole.

Figure 9 shows the variation of the terrain along the rover traverse introduced in Section 2 in terms of the standard deviation of all pixels within the circle covered by the horizontal uncertainty of the rover as well as the absolute variation between the minimum and maximum height experienced within the selected pixels. Note that both the standard deviation and absolute deviation considering a receiver uncertainty of 10 meters are fairly low (below 5 meters in most of the epochs). However, increasing the rover standard deviation to 100 meters, the absolute variation attains significant values (e.g. above 50 meters), nevertheless, the standard deviation remains low.

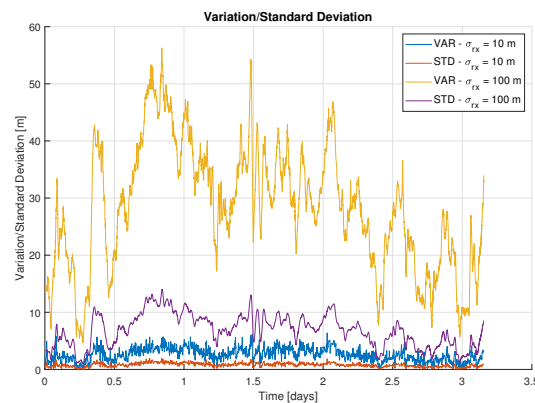


Figure 9. Variation of the terrain along the traverse of the rover considering both the standard deviation (STD) and the absolute deviation (VAR) considering a rover horizontal uncertainty of both 10 meters and 100 meters.

The overall DEM uncertainty is modelled by Equation 14 which contains the terms σ_{Data} and σ_{Rover} which respectively represent the uncertainty related to the data component (i.e. interpolation and orbital errors) as well as the DEM uncertainty induced by the rover horizontal uncertainty (which is defined as the standard deviation of all the pixels that are captured within a circle surrounding the propagated rover position consistent with Figure 7). σ_{Data} and σ_{rover} are assumed uncorrelated.

$$\sigma_{DEM} = \sqrt{\sigma_{Data}^2 + \sigma_{rover}^2} \quad (14)$$

Finally, Table 8 shows the parameters used in the DEM scenario. A threshold is used to disable the DEM aiding in case the current position uncertainty is too large. In such case the uncertainty of the receiver would lead to meaningless results. Furthermore, the n denotes the multiple of σ_{DEM} (i.e. 3-sigma for $n = 3$) used in the measurement covariance matrix Σ_k to account for the geological error component.

Table 8. Main results highlighting the gain in performance when using a DEM.

Parameter	Value
Threshold to enable DEM measurement	150 meter
Multiplier n for σ_{DEM}	3

5. Results

5.1. Baseline

As indicated in Section 4.3, the positioning algorithms used for both the baseline solution (LCNS only) and the solution considering the DEM are similar (i.e. the same measurement model and process noise are used). The only difference occurs when the number of satellites is less than 4, in which case the range-rate observations are no longer used (as these require an accurate estimation of the clock drift).

This section shows the results of the covariance analysis using the simulation parameters defined in Section 4.4. Figure 10 (a) shows the number of visible satellites during the full scenario of approximately 3.1 days, while Figure 10 (b) shows the horizontal dilution of precision (HDOP) of the solution with (red line) and without (blue line) the utilisation of DEM together with the LCNS measurements.

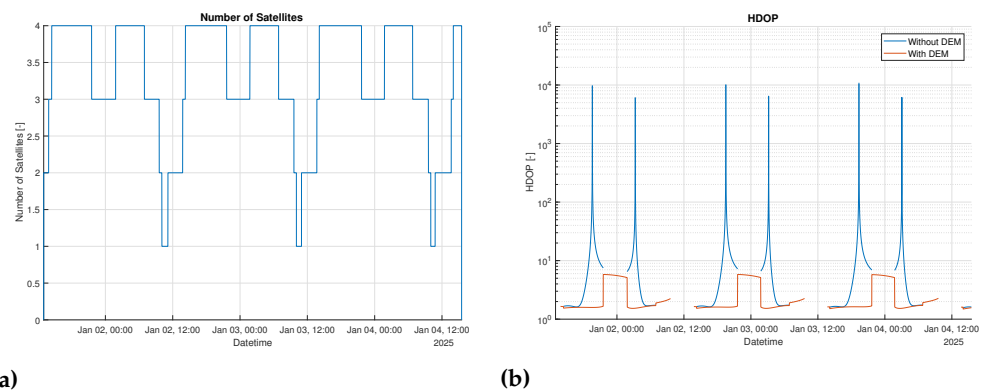


Figure 10. Geometry of the scenario. (a) shows the number of visible satellites in time, while (b) shows the HDOP considering both the LCNS only and LCNS + DEM scenarios.

It can be clearly seen that the LCNS constellation introduced in Table 1 is optimized to ensure good coverage in the South pole as 52 % of the time at least 4 satellites are visible. When comparing the HDOP of the solution with and without DEM, the added value of the DEM measurement is evident. While the HDOP of the satellite only solution (without DEM) has peaks that reach values up to 10⁴, the HDOP when using an additional DEM measurement is always below 10. Furthermore, the availability can be extended to the periods in which only 3 satellites are available, as the 3 satellite measurements and the additional DEM measurement allow the receiver to solve its three dimensional position and clock bias. When less than 3 satellites are available no solution is computed, so no HDOP is provided.

It is important to note that, within this contribution, it is assumed that the rover will continue moving even when no LCNS based solution is available. This is possible using just IMU based propagation or a visual based odometer. When more than 3 satellites are again visible the LCNS based solution is re-started, considering the initial uncertainties in Table 6.

Figure 11 (a) shows the horizontal (2D) covariance of with (red line) and without (blue) the utilisation of the DEM. The behaviour of the horizontal covariance closely follows the behaviour of the HDOP as reported in Figure 10 (b). The peaks at the beginning of each tracking period starting at 300 meter (note that Figure 11 (a) reports 3-sigma) indicate the convergence time needed as the filter is initialized at a position uncertainty of 100 meter (as reported in Table 6). During the periods of good HDOP (satellite only), the performances between the satellite only and satellite and DEM solution are very similar, however in case the geometry of the solution with the satellites degrades, having the DEM in the solution avoids a degradation of the solution accuracy. Furthermore, when only 3 satellites are visible, the LCNS only solution cannot be computed, while with the additional DEM measurement, the rover is able to determine its position with reasonable performance (around 75 meter 3-sigma).

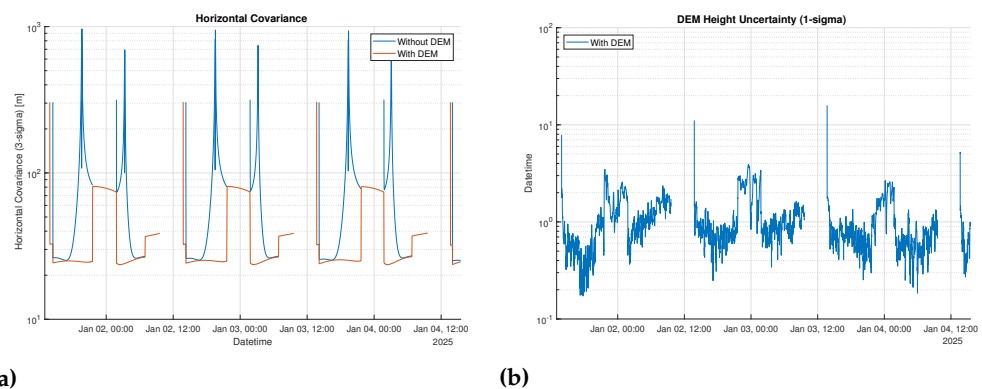


Figure 11. Performance of the LCNS position solution. **(a)** shows the horizontal (2D) covariance (3-sigma) of both the LCNS only as well as the LCNS and DEM solution, while **(b)** shows the 1-sigma uncertainty of the DEM measurement

Figure 11 (b) shows the uncertainty (1-sigma) of the DEM measurement. The peaks (around 10 meter) are caused by the initial rover uncertainty which is set to 100 meter (refer to Table 6) at the beginning of each tracking period. Once the receiver covariance has converged, it can be seen the DEM uncertainty is primarily governed by the data component (refer to Section 4.5.2 for the definition of the data component) which is distributed between 0 and 1 meter (refer to Figure 8 (b)). Nevertheless, in the periods in which only three satellites are available the rover uncertainty attains values above 10 meters (related to the degraded HDOP) such that the rover induced DEM covariance increases as shown in Figure 11 (b).

Table 9 shows the statistics for the rover positioning with and without the usage of DEMs. It can be clearly seen that all statistics reported in Table 9 improve substantially when introducing the additional DEM observation into the positioning algorithm. The availability (e.g. percentage of the time the rover can determine its position) is increased from 52 % to 82 % as the rover is able to determine its position with only 3 satellites when using the DEM. Furthermore, as also shown in Figure 11, the two periods in which 4 satellite are visible are now connected. As such the period of continuous availability increases from slightly more than 5 hours to almost 20 hours. Note, as mentioned earlier, that the visibility window is expected to be better with the optimized orbital parameters under definition in the LCNS Phase A/B1 studies. Finally, the 68, 95 and 99.7 percentiles² of the horizontal position covariance are provided. As expected, the covariance is significantly reduced by constraining the vertical domain with a very accurate measurement.

² Note that these percentiles consider the variation in time of the horizontal covariance (3-sigma) over the traverse

Table 9. Statistics highlighting the gain in performance when using a DEM. The percentiles refer to the time series of the horizontal uncertainty (3-sigma)

Scenario	Availability [%]	Longest Continuous Availability [hr]	68-Percentile [m]	95-Percentile [m]	99.7-Percentile [m]
1. Without DEM	52.0	5.2	80.3	242.8	810.2
2. With DEM	82.2	19.9	37.2	80.3	81.0

Figure 12 shows the cumulative density function (CDF) of the time variation of the horizontal covariance (3-sigma) for both the baseline (i.e. LCNS only) and improved configuration (LCNS + DEM). While CDF is quite similar at lower uncertainties (until a CDF of 0.5), the CDF for the improved configuration (LCNS + DEM) is shifted to the left with respect to the baseline configuration (LCNS only) mainly related to the improvement in geometry due to the additional DEM measurement.

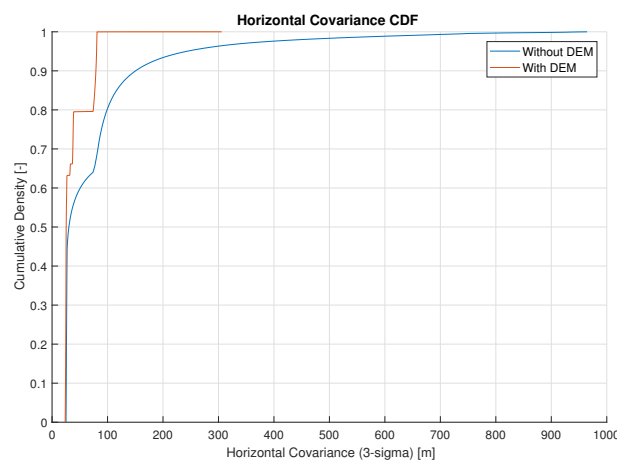


Figure 12. Cumulative density function of the 3-sigma horizontal covariance (considering the time domain).

5.2. Sensitivity Analysis ODTs

To understand the impact of the ODTs uncertainty on the attainable positioning a sensitivity analysis was performed, considering the values reported in Table 6 both as 1-sigma and 3-sigma³. Figure 13 (a) shows the horizontal covariance (3-sigma) of the lunar surface rover considering the baseline and improved ODTs uncertainties as indicated in Table 10. When using the improved scenario, the covariance is reduced by approximately 8 meter (3-sigma) when the position has converged (in case of 4 visible satellites). For the slots in which 3 satellites are visible this reduction is approximately 30 meter (3-sigma).

Table 10. ODTs uncertainty definition per scenario type.

Scenario	Position [m]	Velocity [m/s]	Clock Bias [m]	Clock Drift [m/s]
1. Baseline (1-sigma ³)	15	0.15	10	0.1
2. Improved (3-sigma ³)	5	0.05	3.333	0.033

³ The ODTs uncertainty reported in Table 6 is the baseline for both scenarios. In the first scenario (i.e. baseline) these values are considered as 1-sigma and are used directly in the simulation. In the second scenario (i.e. improved) these values are considered 3-sigma and therefore divided by 3 before they are used in the simulation (note that the simulator uses always the 1-sigma values).

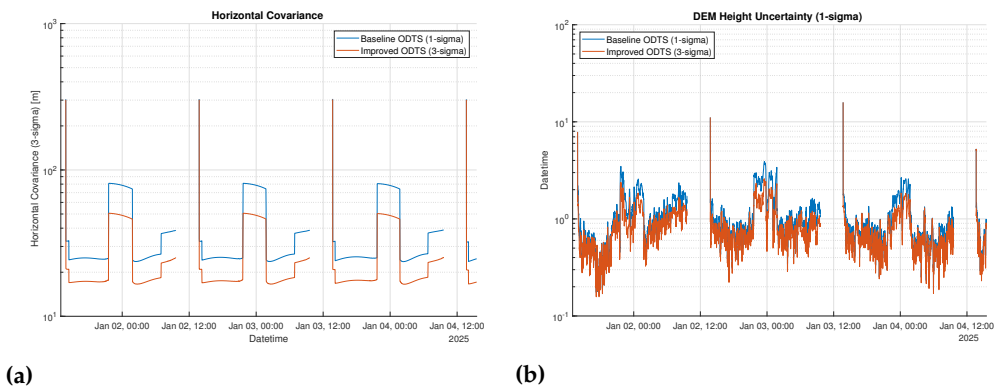


Figure 13. Performance of the LCNS position solution. **(a)** shows the horizontal (2D) covariance of both the LCNS only as well as the LCNS and DEM solution, while **(b)** shows the 1-sigma uncertainty of the DEM measurement

An improvement of the ODS accuracy affects the accuracy of the DEM measurement as shown in Figure 13 (b). When only 3 satellites are visible, the horizontal covariance is smaller for the improved ODS scenario. As such the number of pixels considered to determine the variation of the terrain around the rover is smaller which result in a smaller uncertainty of the DEM measurement.

Table 11 shows the statistics of the ODS sensitivity analysis. Consistently with Figure 13 the 68, 95 and 99.7 percentiles show significant improvements as a result of the improved ODS accuracy.

Table 11. Statistics highlighting the improved position accuracy in case of an improved ODS accuracy. The percentiles refer to the time series of the horizontal uncertainty (3-sigma).

Scenario	68-Percentile [m]	95-Percentile[m]	99.7-Percentile[m]
1. Baseline ODS	37.2	80.3	81.0
2. Improved ODS	23.4	50.1	50.6

5.3. Sensitivity Analysis Process Noise

As previously discussed in Section 4.2, the selection of the process noise matrix Q has a large impact on the attainable position accuracy. Therefore, this section shows the results of the sensitivity analysis for these critical parameters. Table 12 shows three different scenarios for the selection of process noise. The first scenario is in line with the definition of the process noise provided in Table 6 which assumes a relatively low quality IMU. Note that this level of process noise is in line with [29,33] assuming a tactical grade IMU. However, the values used in the previous publications are considered conservative for a tactical grade IMU. Therefore, in this paper we aim to consider a more realistic process noise definition. The second and third scenario correspond to respectively a tactical and navigation grade IMU. Detailed characteristics of both types of IMU can be found in Table 4. The process noise for position and velocity is set to $5 \cdot 10^{-5}$ (note that these values are obtained from internal studies) characterizing the mismodeling of the kinematic filter. The process noise accounting for the IMU velocity random walk (defined in Table 4) is added to this value leading to the values reported in Table 12, consistently with the definition of the process noise for a tightly coupled GNSS/INS filter [47].

Table 12. Process noise definition per scenario type.

Scenario	σ_p [m/√s]	σ_v [m/s/√s]	$\sigma_{\delta t}$ [m/√s]	$\sigma_{\delta \dot{t}}$ [m/s/√s]
1. Baseline	0.01	0.15	1	10
2. Improved (Tactical Grade IMU)	$5 \cdot 10^{-5}$	$3.9 \cdot 10^{-4}$	1	10
3. Improved (Navigation Grade IMU)	$5 \cdot 10^{-5}$	$1.3 \cdot 10^{-4}$	1	10

Figure 14 (a) shows the horizontal covariance (3-sigma) for the three scenarios introduced in Table 12. It can be observed that the difference in attainable position accuracy between scenario 1 (baseline) and scenario 3 (navigation grade IMU) is almost an order of magnitude for the periods in which only 3 satellites are visible (Figure 10 (a)). For the epochs in which 4 satellites are visible, the impact is less pronounced but still significant (approximately 20 meters).

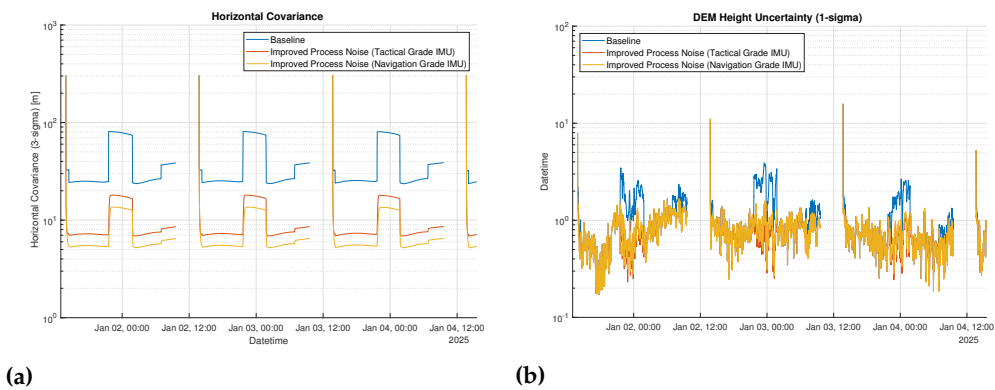


Figure 14. Performance of the LCNS position solution. (a) shows the horizontal (2D) covariance of for the different process noise scenarios identified in Table 12, while (b) shows the 1σ uncertainty of the DEM measurement for the different process noise scenarios identified in Table 12

Figure 14 (b) shows the uncertainty of the DEM measurement. Similarly as for the baseline scenario, the DEM uncertainty is primarily governed by the data component in case 4 satellites are available (as the horizontal uncertainty is within 5 meters). However, contrary to the baseline scenario, scenario 2 and 3 (tactical and navigation grade IMU) does not show the increase in the DEM uncertainty measurement during the periods in which only 3 satellites are visible as its horizontal uncertainty is always below 2 meters (except when initializing the EKF).

Finally Table 13 shows the statistics (in terms of the 68, 95 and 99.7 percentiles) of the three scenarios defined in Table 12. In line with Figure 14 (a), a substantial improvement is shown when using a higher grade IMU (i.e. tactical or navigation grade).

Table 13. Statistics highlighting the gain in performance when improving the EKF process noise (by changing the type of IMU). The percentiles refer to the time series of the horizontal uncertainty (3-sigma).

Scenario	68-Percentile [m]	95-Percentile [m]	99.7-Percentile [m]
1. Baseline	37.2	80.3	81.0
2. Improved (Tactical Grade IMU)	8.3	17.9	18.1
3. Improved (Navigation Grade IMU)	6.3	13.5	15.3

5.4. Sensitivity Analysis ODTs and Process Noise

To understand what will be the ultimate achievable accuracy when considering the improved ODTs accuracy (i.e. 15 meter position uncertainty 3-sigma) and a navigation grade IMU (i.e. low process noise), both elements are combined in a single configuration. Figure 15 (a) shows the horizontal covariance (3-sigma) for both the baseline scenario and the scenario considering the improved ODTs and navigation grade IMU. It can be seen that the horizontal covariance (3-sigma) improves by almost one order of magnitude. Furthermore, note that the 3-sigma horizontal covariance is below 10 meters for the complete duration of the traverse (except when the EKF is initialize). Figure 15 (b) shows the DEM height uncertainty. As the horizontal covariance for the improved scenario is below 10 meter, the uncertainty of the DEM measurement is almost uniquely defined by data component.

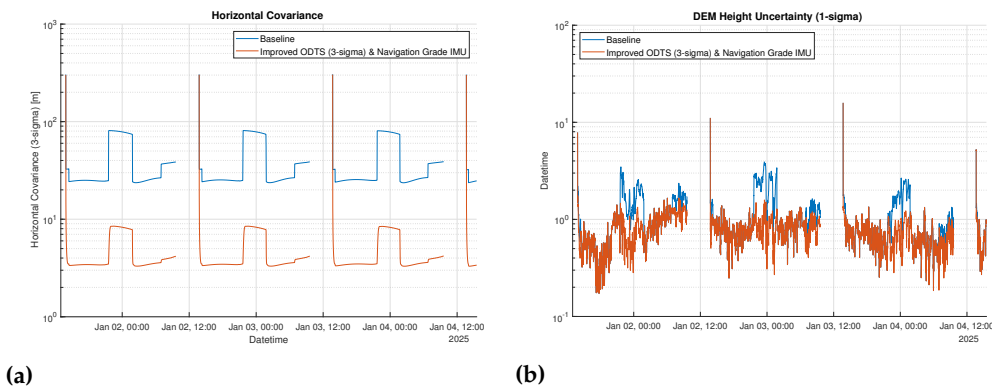


Figure 15. Performance of the LCNS position solution. (a) shows the horizontal (2D) covariance of for the different process noise scenarios identified in Table 12, while (b) shows the 1-sigma uncertainty of the DEM measurement for the different process noise scenarios identified in Table 12

Finally, Table 14 shows the statistics in case of an improved ODTs and navigation grade IMU. In line with Figure 15 (a), a substantial improvement is shown for this configuration resulting in a 3-sigma horizontal covariance which is below 10 meters for (almost) the full duration of the traverse.

Table 14. Statistics highlighting the gain in performance in case of an improved ODTs accuracy and a navigation grade IMU. The percentiles refer to the time series of the horizontal uncertainty (3-sigma).

Scenario	68-Percentile [m]	95-Percentile [m]	99.7-Percentile [m]
1. Baseline	37.2	80.3	81.0
2. Improved ODTs and Tactical Grade IMU	3.9	8.4	8.6

6. Discussion and Conclusions

The global space exploration roadmap assessed the gaps of robotic teleoperation in a report called "Telerobotic control of systems with time delay - Gap assessment report" [48]. One of the challenges identified is the "location accuracy". In the report the authors refer to Earth based GPS/GNSS as one of the options to overcome this gap, but indicate that such a service is not available in the lunar environment. The proposed LCNS system aims to cover this gap providing accurate ranging signals than can be exploited, in real time, targeting both teleoperated or autonomous rovers as discussed this publication.

In this paper we have shown that by constraining the height of the rover, using highly accurate digital elevation models that are available for the lunar South Pole, both the availability and accuracy of a lunar surface rover can be substantially improved. Furthermore, the proposed navigation solution operates under all illumination conditions and allows for very repeatable and autonomous traverse: after the first traverse is performed, all the next

ones can be done fairly autonomously following the same path (as a path free of obstacles is found).

Using the available DEM's, the rover is able to continue to estimate its position while only 3 satellites are in view (contrary to the 4 satellites that are required without such height constraint). This increases the availability of the navigation solution from 52 % to 82 %. Furthermore, by substantially reducing the horizontal dilution of precision (HDOP) by providing an additional measurement in the vertical direction (i.e. a direction which is typically poorly constrained for a satellite based navigation system), the 3-sigma horizontal covariance is reduced from more than 800 meters (considering the 99.7 percentile of the 3-sigma horizontal covariance) to less than 100 meters with very conservative assumptions for the IMU grade and the ODS uncertainty.

A sensitivity analysis showed that an improvement of the LCNS orbit determination and time synchronization (ODTS) accuracy does not have a major impact on the final performances (i.e. an improvement of the 3-sigma horizontal covariance by 8 meters reducing the ODS error by a factor of 3). An improvement of the IMU equipment, however, has a significant impact on the attainable performances, in particular when less than 4 satellites are tracked by the rover. This is expected as the IMU governs the process noise and the capability of the extended Kalman filter (EKF) to tighten the predictions and thus the final performances.

Considering both the improved ODS accuracy and a navigation grade IMU, the 99.7 percentile of the 3-sigma horizontal covariance can be reduced below 10 meters (i.e. 8.6 meters), allowing to be compliant with very stringent user requirement for surface moving rovers (e.g. NASA Lunar Communication Relay and Navigation services requirement LCRNS.3.0570, [49]). Note that the accuracy provided in this publication (3-sigma horizontal covariance) provides a first order estimation on the type of accuracy that can be expected for a lunar rover using LCNS and DEM's to determine its position.

Considering the navigation grade IMU, the final user position is mostly limited by the uncertainty on the DEM data component. This is intrinsic to the DEM data and in principle LCNS cannot provide a direct support to reduce it. However, LCNS can support future LOLA like instruments, providing precise ranging data to improve the precise orbit determination of the satellites hosting the altimeter instrument and iteratively improve the DEM accuracy.

Even if variance-covariance analysis has some limitations (e.g. biases are not modelled), the use of 3-sigma in all error contributions allows to overbound stochastically the user accuracy capable of including a certain margin of biases coupled with the corresponding 1-sigma standard deviation.

This publication has shown that a simple 4 satellite constellation in lunar orbit and a user LCNS receiver that account for DEM and IMU measurements allow to achieve performances below 10 meter 99.7 percent of the time over the traverse considered in this publication. Such performances meet the very stringent requirements expressed by space agencies and commercial users, allowing for larger autonomy and more safety in future lunar rover.

7. Disclaimer

This publication does not cover the final Moonlight constellation, signals and service, but rather presents what could be achieved with a lunar navigation satellite system. The actual Moonlight constellation, signals and related services will be defined as part of ESA programmes, outside this publication.

Abbreviations

The following abbreviations are used in this manuscript:

AOD	Age of Data
BPSK	Binary Phase Shift Keying
CDF	Cumulative Density Function
CPU	Central Processing Unit
DEM	Digital Elevation Model
DLL	Delay Locked Loop
DOP	Dilution of Precision
DSN	Deep Space Network
EIRP	Effective Isotropic Radiated Power
EKF	Extended Kalman Filter
ELFO	Elliptical Lunar Frozen Orbit
ESA	European Space Agency
FLL	Frequency Locked Loop
GITL	Ground-in-the-Loop
GNSS	Global Navigation Satellite System
GPS	Global Positioning System
HDOP	Horizontal Dilution of Precision
IMU	Inertial Measurement Unit
JAXA	Japan Aerospace Exploration Agency
JDR	Joint Doppler and Ranging
LCNS	Lunar Communication and Navigation Services
LiASON	Linked Autonomous Interplanetary Satellite Orbit Navigation
LIDAR	Light Detection and Ranging
LNA	Low Noise Amplifier
LOLA	Lunar Orbiter Laser Altimeter
LRO	Lunar Reconnaissance Orbiter
MER	Mars Exploration Rovers
NASA	National Aeronautics and Space Administration
OCXO	Oven Controlled Crystal Oscillator
ODTS	Orbit Determination and Time Synchronization
PDS	Planetary Data System
PLL	Phase Locked Loop
PNT	Position Navigation and Timing
RF	Radio Frequency
RFFE	Radio Frequency Front-End
SDD	Service Definition Document
SFCG	Space Frequency Coordination Group
SISE	Signal-in-Space Error
SPR	Small Pressurized Rover
VO	Visual Odometry

References

1. International Space Exploration Coordination Group. *The Global Exploration Roadmap*, 2018. Available online: https://www.nasa.gov/sites/default/files/atoms/files/ger_2018_small_mobile.pdf (accessed on 13 June 2022).

2. Johnson, A.E.; Montgomery, J.F. Overview of terrain relative navigation approaches for precise lunar landing. In Proceedings of the 2008 IEEE Aerospace Conference. IEEE, 2008, pp. 1–10.

3. European Space Agency. *Moonlight: connecting Earth with the Moon*, 2020. Available online: https://www.esa.int/ESA_Multimedia/Videos/2020/11/Moonlight_connecting_Earth_with_the_Moon/%28lang%29 (accessed on 23 June 2022).

4. Lockheed Martin. *Communicating with the Moon is Getting Easier*, 2022. Available online: <https://www.lockheedmartin.com/en-us/news/features/2021/lunar-communication-and-navigation-network.html> (accessed on 21 June 2022).

5. GPS World. *Ark Edge Space to study lunar positioning, communications for JAXA*, 2022. Available online: <https://www.gpsworld.com/ark-edge-space-to-study-lunar-positioning-communications-for-jaxa/> (accessed on 21 June 2022).

6. GPS World. *Russia plans to place positioning satellites around the Moon*, 2018. Available online: <https://www.gpsworld.com/russia-plans-to-place-positioning-satellites-around-the-moon/> (accessed on 21 June 2022).

7. China.org.cn. *China starts engineering development of lunar exploration program's fourth phase*, 2022. Available online: http://www.china.org.cn/china/2022-04/25/content_78185065.htm (accessed on 21 June 2022).

8. Draft LunaNet Interoperability Specifications. Technical report, NASA, 2022. Available online: <https://esc.gsfc.nasa.gov/static-files/Draft%20LunaNet%20Interoperability%20Specification%20Final.pdf> (accessed on 21 June 2022).

9. Trexler, T.T.; Odden, R.B. Lunar Surface Navigation. *IEEE Transactions on Aerospace and Electronic Systems* **1966**, AES-2, 252–259.
10. Yenilmez, L.; Temeltas, H. Autonomous navigation for planetary exploration by a mobile robot. In Proceedings of the International Conference on Recent Advances in Space Technologies, 2003. RAST'03. Proceedings of. IEEE, 2003, pp. 397–402.
11. Li, R.; Squyres, S.W.; Arvidson, R.E.; Archinal, B.A.; Bell, J.; Cheng, Y.; Crumpler, L.; Des Marais, D.J.; Di, K.; Ely, T.A.; et al. Initial results of rover localization and topographic mapping for the 2003 Mars Exploration Rover mission. *Photogrammetric Engineering & Remote Sensing* **2005**, 71, 1129–1142.
12. Li, R.; Di, K.; Howard, A.B.; Matthies, L.; Wang, J.; Agarwal, S. Rock modeling and matching for autonomous long-range Mars rover localization. *Journal of Field Robotics* **2007**, 24, 187–203.
13. Maimone, M.; Johnson, A.; Cheng, Y.; Willson, R.; Matthies, L. Autonomous navigation results from the Mars Exploration Rover (MER) mission. In *Experimental robotics IX*; Springer, 2006; pp. 3–13.
14. Goldberg, S.B.; Maimone, M.W.; Matthies, L. Stereo vision and rover navigation software for planetary exploration. In Proceedings of the Proceedings, IEEE aerospace conference. IEEE, 2002, Vol. 5, pp. 5–5.
15. Geromichalos, D.; Azkarate, M.; Tsardoulas, E.; Gerdes, L.; Petrou, L.; Perez Del Pulgar, C. SLAM for autonomous planetary rovers with global localization. *Journal of Field Robotics* **2020**, 37, 830–847.
16. Carle, P.J.; Barfoot, T.D. Global rover localization by matching lidar and orbital 3d maps. In Proceedings of the 2010 IEEE International Conference on Robotics and Automation. IEEE, 2010, pp. 881–886.
17. Matthies, L.; Daftry, S.; Tepsuporn, S.; Cheng, Y.; Atha, D.; Swan, R.M.; Ravichandar, S.; Ono, M. Lunar Rover Localization Using Craters as Landmarks. *arXiv preprint arXiv:2203.10073* **2022**.
18. Jun, W.W.; Cheung, K.M.; Lightsey, E.G.; Lee, C. A minimal architecture for real-time lunar surface positioning using joint Doppler and ranging. *IEEE Transactions on Aerospace and Electronic Systems* **2021**, 58, 1367–1376.
19. Parker, T.; Golombek, M.; Powell, M. Geomorphic/geologic mapping, localization, and traverse planning at the Opportunity landing site, Mars. In Proceedings of the 41st Annual Lunar and Planetary Science Conference, 2010, number 1533 in Lunar and Planetary Science Conference, p. 2638.
20. Chelmins, D.T.; Welch, B.W.; Sands, O.S.; Nguyen, B.V. A kalman approach to lunar surface navigation using radiometric and inertial measurements. Technical report, NASA, 2009.
21. Hesar, S.G.; Parker, J.S.; Leonard, J.M.; McGranaghan, R.M.; Born, G.H. Lunar far side surface navigation using linked autonomous interplanetary satellite orbit navigation (LiAISON). *Acta Astronautica* **2015**, 117, 116–129.
22. Allender, E.J.; Orgel, C.; Almeida, N.V.; Cook, J.; Ende, J.J.; Kamps, O.; Mazrouei, S.; Slezak, T.J.; Soini, A.J.; Kring, D.A. Traverses for the ISECG-GER design reference mission for humans on the lunar surface. *Advances in space research* **2019**, 63, 692–727.
23. Li, S.; Lucey, P.G.; Milliken, R.E.; Hayne, P.O.; Fisher, E.; Williams, J.P.; Hurley, D.M.; Elphic, R.C. Direct evidence of surface exposed water ice in the lunar polar regions. *Proceedings of the National Academy of Sciences* **2018**, 115, 8907–8912.
24. Smith, D.E.; Zuber, M.T.; Jackson, G.B.; Cavanaugh, J.F.; Neumann, G.A.; Riris, H.; Sun, X.; Zellar, R.S.; Coltharp, C.; Connelly, J.; et al. The lunar orbiter laser altimeter investigation on the lunar reconnaissance orbiter mission. *Space science reviews* **2010**, 150, 209–241.
25. Tooley, C.R.; Houghton, M.B.; Saylor, R.S.; Peddie, C.; Everett, D.F.; Baker, C.L.; Safdie, K.N. Lunar Reconnaissance Orbiter mission and spacecraft design. *Space Science Reviews* **2010**, 150, 23–62.
26. Barker, M.K.; Mazarico, E.; Neumann, G.A.; Smith, D.E.; Zuber, M.T.; Head, J.W. Improved LOLA elevation maps for south pole landing sites: Error estimates and their impact on illumination conditions. *Planetary and Space Science* **2021**, 203, 105119.
27. Neumann, G.A. Lunar Reconnaissance Orbiter Lunar Orbiter Laser Altimeter reduced data record and derived products software interface specification, version 2.42, LRO-L-LOLA-4-GDR-V1.0, NASA Planetary Data Ssystem (PDS), 2011. Available online: https://pds-geosciences.wustl.edu/lro/lro-l-lola-3-rdr-v1/lrolol_1xxx/document/rdrsis.pdf (accessed on 21 June 2022).
28. Delépaut, A.; Giordano, P.; Ventura-Traveset, J.; Blonski, D.; Schönfeldt, M.; Schoonejans, P.; Aziz, S.; Walker, R. Use of GNSS for lunar missions and plans for lunar in-orbit development. *Advances in Space Research* **2020**, 66, 2739–2756.
29. Grenier, A.; Giordano, P.; Bucci, L.; Cropp, A.; Zoccarato, P.; Swinden, R.; Ventura-Traveset, J. Positioning and Velocity Performance Levels for a Lunar Lander using a Dedicated Lunar Communication and Navigation System. *NAVIGATION: Journal of the Institute of Navigation* **2022**, 69.
30. Barker, M.; Mazarico, E.; Neumann, G.; Zuber, M.; Haruyama, J.; Smith, D. A new lunar digital elevation model from the Lunar Orbiter Laser Altimeter and SELENE Terrain Camera. *Icarus* **2016**, 273, 346–355.
31. Barton, G.H.; Sheppard, S.W.; Brand, T.J. Proposed autonomous lunar navigation system. *Astrodynamics 1993* **1993**, pp. 1717–1736.
32. Schönfeldt, M.; Grenier, A.; Delépaut, A.; Giordano, P.; Swinden, R.; Ventura-Traveset, J. Across the lunar landscape: Towards a dedicated lunar PNT system. *Inside GNSS* **2020**.
33. Giordano, P.; Grenier, A.; Zoccarato, P.; Bucci, L.; Cropp, A.; Swinden, R.; Gomez Otero, D.; El-Dali, W.; Carey, W.; Duvet, L.; et al. Moonlight navigation service-how to land on peaks of eternal light. In Proceedings of the Proceedings of the 72nd International Astronautical Congress (IAC), 2021.
34. Space Frequency Coordination Group. *Communication AND Positioning, Navigation, and Timing Frequency Allocations and Sharing in the Lunar Region*, 2021. Available online: [https://www.sfcgonline.org/Recommendations/REC%20SFCG%2032-2R3%20\(Freq%20for%20Lunar%20region\).pdf](https://www.sfcgonline.org/Recommendations/REC%20SFCG%2032-2R3%20(Freq%20for%20Lunar%20region).pdf) (accessed on 14 June 2022).

35. Giordano, P.; Melman, F.; Swinden, R.; Zoccarato, P.; Ventura-Traveset, J. The Lunar Pathfinder PNT Experiment and Moonlight Navigation Service: The Future of Lunar Position, Navigation and Timing. In Proceedings of the Proceedings of the 2022 International Technical Meeting of The Institute of Navigation, 2022, pp. 632–642.
36. Northrop Grumman. *LN-200S: Inertial Measurement Unit (IMU)*, 2021. Available online: <https://www.axtal.com/cms/docs/doc124949.pdf> (accessed on 20 June 2022).
37. Airbus Defense and Space. *Emphasis: Empowering Heterogeneous Aviation Through Cellular Signals - Deliverable D5.3 - INS/GNSS Fusion*, 2018. Available online: <https://ec.europa.eu/research/participants/documents/downloadPublic?documentIds=080166e5c206c883&appId=PPGMS> (accessed on 14 June 2022).
38. iMAR. *iNAV-RQH-1001*, 2014. Available online: https://www.imar-navigation.de/downloads/NAV_RQH_1001_en.pdf (accessed on 21 June 2022).
39. Vectron Oscillators. *OX-249 Space Qualified Oven Controlled Crystal Oscillator (OCXO)*, 2021. Available online: <https://www.vectron.com/products/ocxo/OX-249.pdf> (accessed on 14 June 2022).
40. AXTAL GmbH. *AXIOM6060: Ultra-Low Phase Noise 100 MHz OCXO for Space Application*, 2015. Available online: <https://www.axtal.com/cms/docs/doc91629.pdf> (accessed on 14 June 2022).
41. AXTAL GmbH. *AXIOM70SL: Ultra-Low Phase Noise 10 MHz OCXO with HCMOS output for Space Application (Space COTS version)*, 2022. Available online: <https://www.axtal.com/cms/docs/doc124949.pdf> (accessed on 14 June 2022).
42. BROWN, R.; HWANG, P. Introduction to random signals and applied Kalman filtering(Book). New York, John Wiley & Sons, Inc., 1992. 512 **1992**.
43. Montenbruck, O.; Gill, E. *Satellite orbits*; Springer, 2013.
44. European Commission. *European GNSS (Galileo) Open Service Definition Document*, 2021. Available online: https://www.gsc-europa.eu/sites/default/files/sites/all/files/Galileo-OS-SDD_v1.2.pdf (accessed on 14 June 2022).
45. Petovello, M.; Cannon, M.; Lachapelle, G. Benefits of using a tactical-grade IMU for high-accuracy positioning. *NAVIGATION, Journal of the Institute of Navigation* **2004**, 51, 1–12.
46. Kaplan, E.D.; Hegarty, C. *Understanding GPS/GNSS: principles and applications*; Artech house, 2017.
47. Farrell, J. *Aided navigation: GPS with high rate sensors*; McGraw-Hill, Inc., 2008.
48. International Space Exploration Coordination Group. *Telerobotics Control of Systems with Time Delay - Gap Assessment Report*, 2018. Available online: <https://www.globalspaceexploration.org/wordpress/docs/Telerobotic%20Control%20of%20Systems%20with%20Time%20Delay%20Gap%20Assessment%20Report.pdf> (accessed on 14 June 2022).
49. Lunar Communications Relay and Navigation Systems (LCRNS) - Preliminary Lunar Relay Services Requirements Document (SRD). Technical report, NASA, 2022. Available online: <https://esc.gsfc.nasa.gov/static/2fbc056474937c4e3ecfdb1dc595f06/ee60f0dad022948b2e8ce03e6e86a2f0.pdf> (accessed on 24 June 2022).